TET2-Mutant Hematopoietic Clones Shape the Lung Immune Microenvironment in NSCLC Initiation and Progression

Mazzi Moore[1]
Supervisors: Constandina Pospori, M.D., Ph.D.[2], Charles Swanton, M.D., Ph.D.[2,3,4]

[1]Massachusetts Institute of Technology, Boston, Massachusetts, US
[2]Cancer Evolution and Genome Instability Laboratory, The Francis Crick Institute, London, UK
[3]Cancer Research UK Lung Cancer Centre of Excellence, University College London Cancer Institute, London, UK
[4]Department of Medical Oncology, University College London Hospitals, London, UK

ABSTRACT

Clonal hematopoiesis of indeterminate potential (CHIP), an aging-related clonal expansion of hematopoietic cells carrying leukemia-associated mutations in the absence of hematologic malignancies, increases the risk of lung cancer[1,7]. To investigate how CHIP alters the lung immune microenvironment to drive non-small cell lung cancer (NSCLC) initiation and progression, we used organoid assays that isolated alveolar and interstitial macrophage paracrine signaling and modeled EGFR-mutant NSCLC alongside TET2-mutant CHIP in vivo. Macrophage-derived secretions were found to promote organoid initiation, with IL-1β having a positive, concentration-dependent effect on organoid formation, as well as proportional suppression by IFN-γ. In an in-vivo model of CHIP in NSCLC tumor-bearing animals, lung tissue exhibited a more aggressive, spatially disperse EGFR+ architecture, as well as an associated decrease in alveolar macrophages and an expansion of bone marrow-derived myeloid populations. These findings demonstrate CHIP-associated modulation of the lung immune TME in both initiation and progression settings, implicating myeloid signaling pathways in the study and treatment of NSCLC.

I. INTRODUCTION

Clonal hematopoiesis of indeterminate potential (CHIP) is an age-associated condition driven by the clonal expansion of hematopoietic cells carrying somatic, leukemia-associated mutations in the absence of hematologic malignancies[1]. Individuals with CHIP have a 30-40% increase in all-cause mortality[2,3], with implications on several disorders of systemic inflammation[4], including blood cancers and cardiometabolic and liver diseases[1,3,5]. CHIP has also been associated with increased incidence of solid cancers like non-small cell lung cancer (NSCLC)[6,7]. Globally, lung cancer is the most frequently diagnosed cancer and leading cause of cancer death[8], but the mechanistic drivers in never-smokers remain poorly understood: CHIP is an emerging candidate.

CHIP is defined by a 2% variant allele fraction (VAF) of a mutant gene[9], most commonly one of three epigenetic regulator genes: DNMT3A, TET2, and ASXL1[2]. Mutant hematopoietic stem and progenitor cells (HSPCs) with loss of function in these genes are more proliferative than wild-type stem cells and expand within the bone marrow niche, increasing hematopoiesis into myeloid lineages[3,10]. Contributing to a hyperinflammatory environment, the frequently mutated TET methylcytosine dioxygenase 2 (TET2) gene has been shown to drive elevated IL-1β levels, as well as increased chemokine expression and inflammasome activation, in myeloid cells[2,11].

The progeny of TET2-mutant HSPCs are known modulators of the immune and tumor microenvironment in NSCLC[4], with both paracrine secretions and direct contact signaling promoting tumorigenesis[12,13]. Notably, CHIP myeloid cells—most abundantly, macrophages—localize near malignant cells and infiltrate tumor cores at an increased density as compared to wild-type controls[14]. More specifically, recent studies have revealed the preferential migration of TET2-mutant monocytes toward cancer cells and accumulation as CD11b+

monocyte-derived macrophages[12]. Further work is necessary to understand how myeloid localization and the broader immune tumor microenvironment (TME) mechanistically promote lesion growth.

CHIP has also been investigated in the context of exogenous inflammatory insults, suggesting a "two-hit" model of NSCLC initiation[15]. For instance, lipopolysaccharide (LPS) stimulation promotes TET2-mutant macrophage release of IL-1β by priming inflammasomes and enhancing IL-1β gene expression with respect to wild-type control cells[16]. In the study of never-smoking human NSCLC, a well-recognized inflammatory agent is particulate matter ($PM_{2.5}$) air pollution[17]. Long-term $PM_{2.5}$ exposure is associated with NSCLC incidence, attributed to the influx of proinflammatory macrophages releasing IL-1β and subsequent induction of a progenitor state in EGFR-mutant alveolar type II (AT2) cells[18]. The addition of CHIP may exacerbate these findings. In an analysis of never-smoking patients living in above-median $PM_{2.5}$ levels, CHIP is associated with a 3-fold higher risk of NSCLC, as well as heightened markers of inflammation; however, ambient PM exposure is not independently predictive of CHIP[17]. Functional in-vitro and in-vivo studies will help better understand the $PM_{2.5}$-CHIP interplay in the initiation of NSCLC.

Here, we examine the effect of TET2-mutant clonal hematopoiesis, a critical lung cancer risk factor, on EGFR-driven NSCLC initiation and progression. Primary AT2 organoid assays serve as a model of tumor initiation; indirect co-cultures with TET2-mutant alveolar macrophages (AMs) and interstitial macrophages (IMs), as well as direct supplementation with cytokines, provide insight into the protumorigenic capacity of immune paracrine signaling in the presence or absence of $PM_{2.5}$ stimulation. To model long-term effects of CHIP on tumor growth, wild-type and TET2-knockout bone marrow cells are also transplanted into tumor-bearing mice, assessing how TET2-mutant immune cells alter EGFR+ architecture and compartmentalization of the immune TME.

II. MATERIALS AND METHODS

A. Mice

All animal regulated procedures were approved by the Francis Crick Institute Biological Research Facility Strategic Oversight Committee, incorporating the Animal Welfare and Ethical Review Body, conforming with UK Home Office guidelines and regulations under the Animals (Scientific Procedures) Act 1986, including Amendment Regulations 2012. Animals were housed in individually ventilated cages with unlimited access to food and water and a 12-hour light cycle.

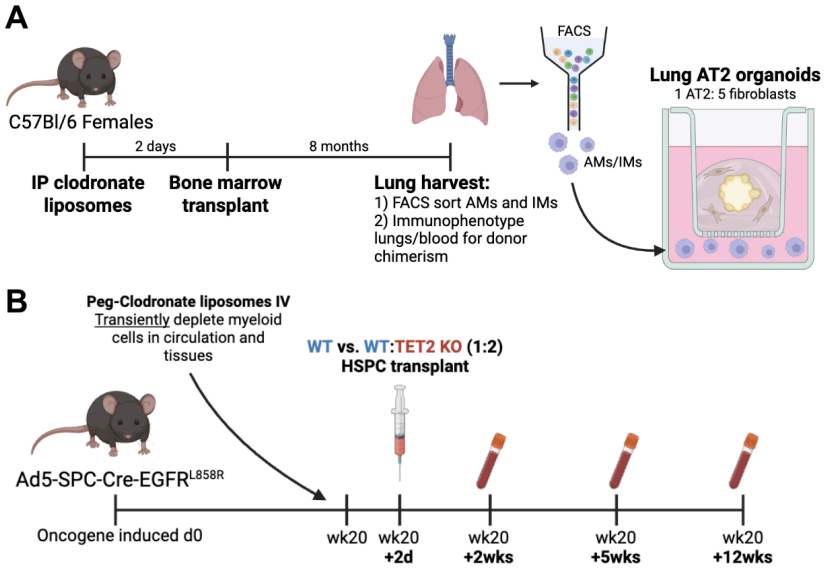

Figure 1. Mouse model schematics

A. Diagram describing IM and AM isolation from mice exposed to a single-dose of clodronate liposomes and transplanted with wild-type or TET2-mutant bone marrow cells, followed by indirect organoid co-culture with 1:5 AT2 cells and fibroblasts.

B. Diagram depicting a tumor-bearing, EGFR-driven NSCLC mouse model. Details PEG-clodronate depletion of circulating and tissue-resident myeloid cells, causing an emergency cascade of granulopoiesis, and subsequent wild-type or 1:2 wild-type:TET2-knockout HSPC transplant.

Graphics designed in BioRender.

For IM and AM organoid co-culture assays, phagocytic immune cells were depleted in C57Bl/6 mice (N=5) via a single intraperitoneal dose of PEG-clodronate liposomes (Figure 1A). 2 days post-depletion, the mice underwent a lineage-negative transplant of wild-type or TET2-knockout bone marrow (BM) cells. Facilitating engraftment and long-term chimerism of IMs and AMs in non-tumor-bearing animals, lungs were subsequently harvested 8 months after the adoptive transfer. Alveolar and interstitial lung macrophages were FACS-sort purified from the lungs, identified by CD3-, CD19-, Ter119-, Ly6C-, Ly6G-, CD64+, and MertK+, with alveolar macrophages designated as CD11c+ and CD11b- and interstitial macrophages as CD11c- and CD11b+. Wild-type and TET2-knockout donor chimerism among IMs and AMs was determined by the proportion of CD45.1+ or CD45.2+ cells in each subset.

In a parallel mouse cohort, Cre-mediated recombination of the EGFR-L858R oncogene was initiated by intratracheal instillation of Ad5-SPC-Cre (2.5 x 10^8 virus particles per 50µl) in female Rosa26$^{LSL\text{-}tTa/LSL\text{-}tdTomato}$;TetO-EGFR^{L858R} mice (N=8) (Figure 1B). 20 weeks later (when small tumors were expected to be established in all animals), the mice were administered a single dose of PEG-clodronate liposomes (200µl IV per mouse), followed by the adoptive transfer of 2M lineage-negative BM cells from wild-type animals or a 1:2 mixture from wild-type and TET2-knockout animals. The expression of congenic markers identified wild-type (CD45.1.2) and TET2-knockout (CD45.1) donor-derived hematopoietic cells, distinguishing them from recipient-derived (CD45.2) cells in FACS analysis of peripheral blood 12 weeks post-transfer. 13 weeks after the BM transfer (33 weeks after oncogene induction), the transplanted, tumor-bearing animals were sacrificed, and lungs were harvested, fixed in 10% NBF for 24 hours, and embedded in paraffin. 7µm lung sections were immunostained with CD3, CD11b, CD68, Ly6G, EGFRL858R, CD31, and Dapi to identify T cells (CD3+), monocytes (CD11b+, CD68-, Ly6G-), neutrophils (CD11b+, Ly6G+, CD68-), alveolar macrophages (CD68+, CD11b-), interstitial macrophages (CD68+, CD11b+), tumor cells (EGFR+), and blood vessels (CD31+).

B. Primary AT2 Isolation and Organoid Initiation Assays

AT2 cells were isolated from CCSP-rtTa;TetO-EGFRL858R animals by FACS sorting CD45-, Ter119-, CD31-, EpCam+, CD49f-, and MHC II + cells from digested lung single-cell suspension. AT2 cells were combined with normal human lung fibroblasts (NHLF cell line obtained from Crick Cell services) at a 1:5 ratio in 3D media (DMEM/F-12 (1:1) (1X), 10% heat-inactivated Fetal Bovine Serum, 1% Penicillin-Streptomycin, 1% Insulin-Transferrin-Selenium, 1µg/mL Doxycycline) and mixed with growth factor reduced (GFR) matrigel (1 volume cell suspension in 3D media:1 volume GFR matrigel). Containing 5,000 AT2 cells and 25,000 fibroblasts, 100µl were plated on the upper chamber of a 0.4µm transwell in a 24-well plate. Doxycycline was added in the GFR matrigel cell suspension and media at the bottom of the transwell chamber at 1µg/mL to induce and maintain expression of the EGFR L858R oncogenic mutation throughout the experiment. Media was half-changed every 2-3 days.

In some experiments, 50,000 AMs or 50,000 IMs (donor+recipient-derived) were plated in the bottom chamber of the transwells (Figure 1A). To create an Air-Liquid-Interface (ALI), 600µl of RPMI 1640 (1x) + GlutaMAX media supplemented with 10% heat-inactivated FBS, 1% Penicillin/Streptomycin and 30ng/ml mGM-CSF, 10ng/ml hTGFb1, 1µM Rosiglitazone, and 1µg/mL Doxycycline was added to the bottom chamber of the transwell. All IM

cultures were administered a single treatment of 12.5µg/mL $PM_{2.5}$; AM cultures received either PBS or a single treatment of 12.5µg/mL $PM_{2.5}$. On day 14, representative ROI images of the IMs were captured on the Zeiss Observer Z1, followed by harvest and counting on day 17. Representative ROI images of the AMs were also captured on the Observer microscope on day 14, followed by same-day harvest and counting on day 14 (Figure 2). All organoid-containing transwells were transitioned to fresh wells with 3D organoid media only on day 14 through day 17 to facilitate expansion of small cell clusters (Figure 2). The organoids were imaged with the Observer microscope, and organoid number was quantified on QuPath v0.6.0.

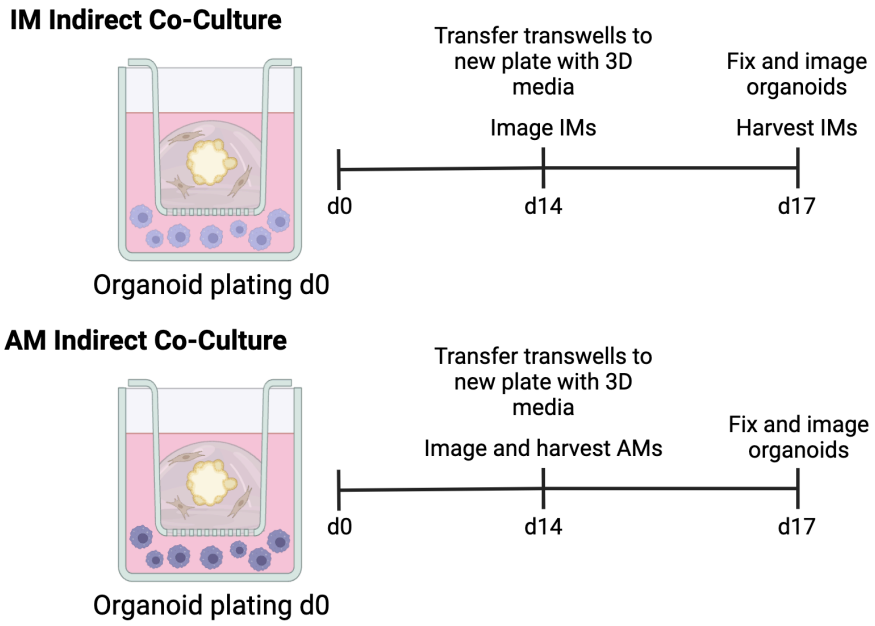

Figure 2. IM and AM organoid co-culture schematics
Diagram describing IM and AM indirect co-culture harvest and imaging timelines.
Graphics designed in BioRender.

In further experiments, the described AT2-fibroblast transwells were plated in 600µl of 3D media and titrated concentrations of IL-1β (no IL-1β, 2pg/mL, 20pg/mL, 200pg/mL, 2ng/mL), in either the absence or presence of 10ng/mL IFN-γ. Organoid cultures were imaged with the Zeiss Observer Z1 on day 14, and organoid number was quantified on QuPath v0.6.0.

C. QuPath Image Analysis Pipeline

The multiplex immunofluorescent lung section images were processed and analyzed in QuPath v0.6.0 (Figure 3). To quantify the total tissue area, mean intensity thresholding was applied across all channels, excluding airspace and other artifacts. Then the built-in QuPath cell detection feature was applied to the mean DAPI channel with a 5µm expansion, detecting the cells in each lung section. To more specifically classify cell detections as stroma, tumor, or 5 immune subtypes (AMs, IMs, neutrophils, T cells, monocytes), a built-in QuPath AI object classifier was trained on manual annotations across several samples and then validated on a separate cohort of the multiplex fluorescent images.

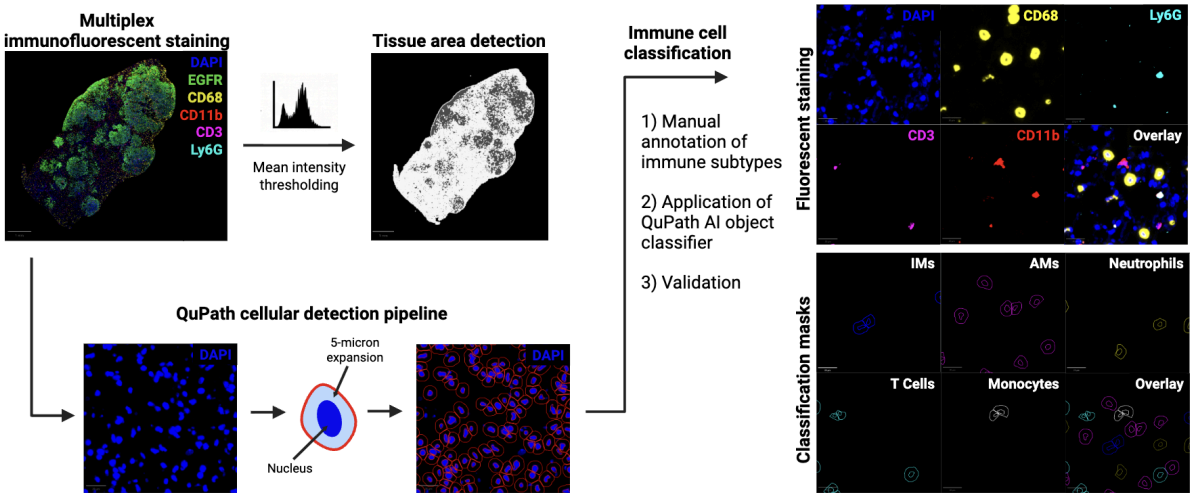

Figure 3. QuPath image analysis pipeline

Schematic of tissue area detection and cell classification QuPath pipeline for multiplex immunofluorescent lung sections.

Graphic designed in BioRender.

To compare the immune TMEs in distinct regions of tumor and tissue morphology, the lung sections were manually annotated on the basis of EGFR+ architecture (Figure 4A). All high-density, EGFR+ lesions with explicit borders were classified as either Compact A or Compact B. Compact A lesions are defined by a lack of breakout and a continuous EGFR+ border; Compact B borders are not fully continuous and may contain breakout regions. Three representative regions, of similar cross-sectional area to the Compact A and B lesions, were also annotated in each sample to characterize EGFR+ Disperse regions and Non-EGFR+ regions. To further refine TME analysis, an invasive margin was also annotated as the 75µm region spanning a 50µm external extension and a 25µm internal extension from the original lesion annotation (Figure 4B).

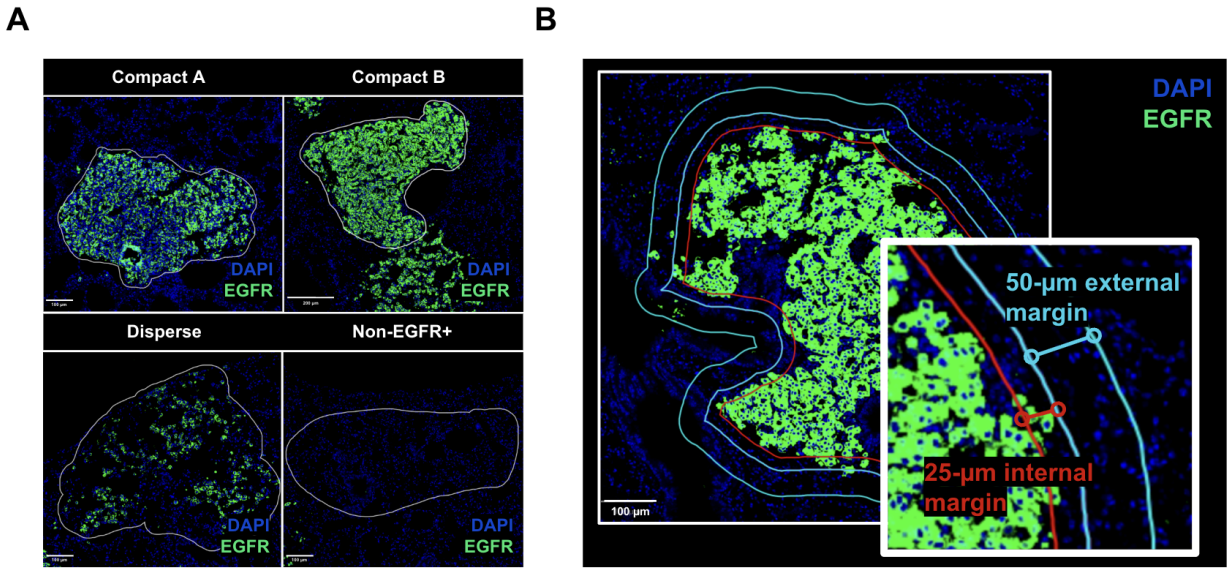

Figure 4. EGFR+ architecture classification; margin annotation

A. Representative immunofluorescent images depicting EGFR+ architecture classifications: Compact A, Compact B, Disperse, Non-EGFR+. Compact A, Disperse, Non-EGFR+ scale bar is 100µm. Compact B scale bar is 200µm.

B. Representative immunofluorescent image of margin annotation, composed of a 50µm external extension and a 25µm internal extension from the original lesion annotation. Scale bar is 100 µm.

D. Statistical Analysis

All statistical analyses were performed using GraphPad Prism Version 11.0.2 (100). For two-condition comparisons, t-tests were used; for multi-condition comparisons, two-way analysis of variance (ANOVA) was performed, followed by Tukey post-hoc tests to compare group means. Data is presented as the mean with the standard error of the mean, and p-values of 0.05 or less were considered statistically significant.

III. RESULTS

A. IL-1β drives AT2 organoid outgrowth; attenuated by IFN-γ co-treatment

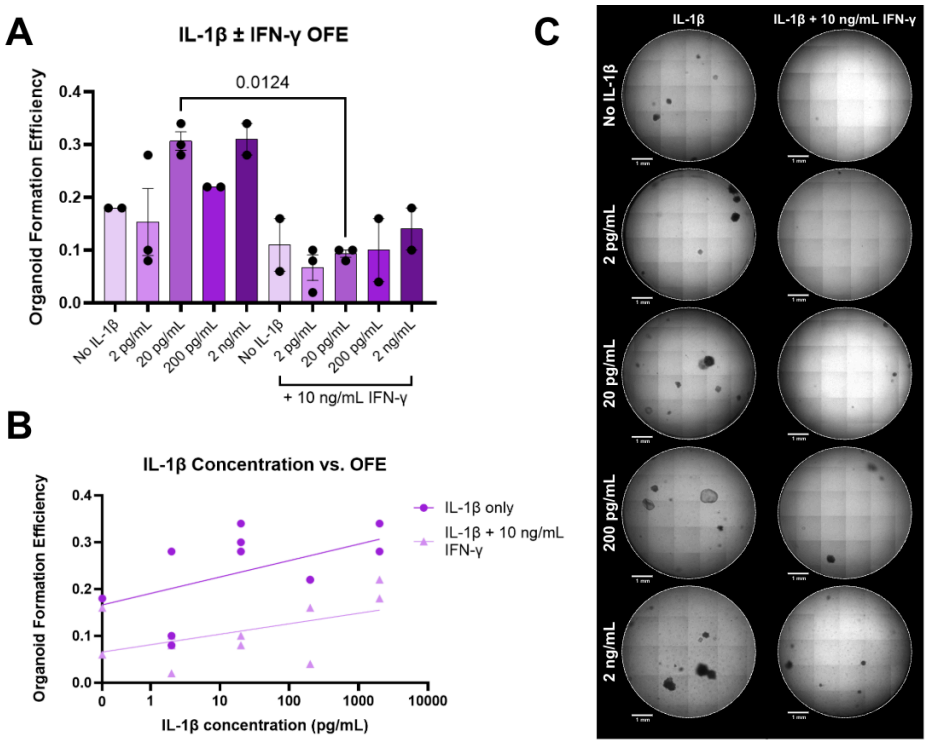

Figure 5. Effect of IL-1β concentration gradient and IFN-γ treatment on organoid formation efficiency

A. Quantification of OFE along an IL-1β gradient with or without 10ng/mL IFN-γ. One-way ANOVA, post-hoc Tukey.

B. Correlation between IL-1β concentration and corresponding OFE along IL-1β only and IL-1β + 10ng/mL IFN-γ titrations. Simple linear regression.

C. Representative brightfield, whole-well images of organoids exposed to an IL-1β gradient in the absence or presence of 10ng/mL IFN-γ. Scale bar is 1mm.

Error bars indicate mean ± SEM.

In primary AT2 organoid models, organoid formation efficiency (OFE)—number of organoids per well divided by 5,000 plated AT2 cells x 100—was compared along an IL-1β gradient and replicate samples treated with 10ng/mL IFN-γ (Figure 5A) (One-way ANOVA $F(5,10)=5.596$, $p=0.0022$, $\eta^2=0.7825$). Increasing IL-1β concentration generally promoted organoid formation, with the presence of IFN-γ numerically suppressing OFE and organoid outgrowth; notably, the average OFE of the 20pg/mL IL-1β samples was significantly elevated with respect to the 20pg/mL IL-1β + 10ng/mL IFN-γ samples ($p=0.0124$). Figure 5B further illustrates a positive correlation between IL-1β concentration and OFE. Although the linear regression of IL-1β only lacked statistical significance ($p=0.1705$), IL-1β + 10ng/mL IFN-γ exhibited an increase in OFE with IL-1β concentration ($F(1,10)=2.181$, $p=0.0085$, $\eta^2=0.5165$). These phenotypes are also reflected in the brightfield, whole-well images in Figure 5C.

B. TET2 mutations promote IM-associated organoid growth and confer proliferative advantage in macrophages

The IMs and AMs plated in the indirect organoid co-cultures were harvested from recipient mice of wild-type or TET2-mutant BM transplants. To ask whether TET2-mutant HSPCs had a proliferative advantage in vivo, Figure 6A exhibits the percent donor chimerism of the harvested immune cells quantified by FACS analysis of congenic markers (One-way ANOVA $F(3,6)=269.4$, $p<0.0001$, $\eta^2=0.993$). The TET2-mutant lung macrophage compartment had greater expansion of donor BM cells as compared to wild-type in both AMs ($p<0.0001$) and IMs ($p<0.0001$).

Figure 6B shows a marked OFE increase in the PM-exposed TET2-mutant IM co-culture with respect to the PM-exposed control ($p<0.0001$) and PM-exposed wild-type IM ($p<0.0001$) conditions (One-way ANOVA $F(3,7)=248.4$, $p<0.0001$, $\eta^2=0.9907$). Figure 6C similarly displays the OFE of the AM co-cultures; while mean and fold-change comparison between the wild-type and TET2-mutant samples lacked statistical significance, the addition of AMs significantly increased organoid formation as compared to PBS and PM controls (One-way ANOVA $F(5,10)=14.66$, $p=0.0002$, $\eta^2=0.8799$). On day 14, the plated IMs and AMs were imaged (Figure 6D), with greater expansion observed in the TET2-mutant IMs. On day 17 and day 14, IMs and AMs, respectively, were harvested and counted to assess yield from the 50,000 macrophages originally plated. TET2-mutant IMs had a significantly higher yield compared to wild-type ($t(3)=8.662$, $p=0.0032$, $\eta^2=0.962$) (Figure 6E). Although not statistically significant, TET2-mutant cultures yielded higher AM expansion in both PBS and PM conditions as compared to wild-type, with PM exposure resulting in a lower yield across both genotypes (One-way ANOVA $F(9,13)=2.486$, $p=0.0663$, $\eta^2=0.6325$) (Figure 6F).

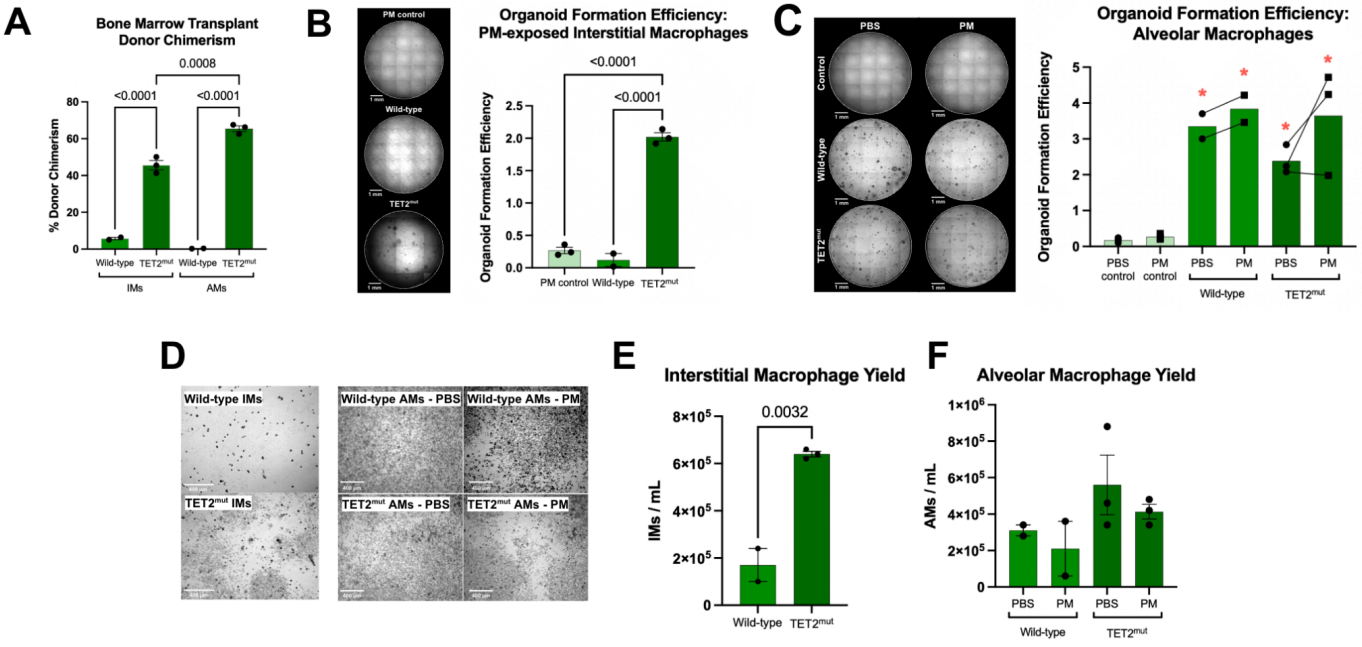

Figure 6. Organoid growth in AT2 indirect co-cultures; interstitial and alveolar macrophage expansion

A. Comparison of donor chimerism in lung IM and AM compartment of recipient mice after transplant of wild-type or TET2-mutant BM cells. One-way ANOVA, post-hoc Tukey.

B. LEFT: Representative brightfield, whole-well organoid images of PM control and indirect co-cultures with PM-exposed wild-type IMs and PM-exposed TET2-mutant IMs. Scale bar is 1mm. RIGHT: Quantification of OFE in AT2 organoids following co-culture with PM-exposed wild-type and TET2-mutant IMs. One-way ANOVA, post-hoc Tukey.

C. LEFT: Representative brightfield, whole-well organoid images of PBS- or PM-stimulated control and wild-type and TET2-mutant AM co-cultures. Scale bar is 1mm. RIGHT: Quantification of OFE in AT2 organoids following co-culture with PBS- or PM-exposed wild-type and TET2-mutant AMs. Connection lines link AMs from the same mouse. * denotes $p<0.05$ statistical significance to both the PBS control and the PM control. One-way ANOVA, post-hoc Tukey.

D. LEFT: Representative brightfield images of wild-type and TET2-mutant IMs exposed to 12.5µg/mL $PM_{2.5}$ before harvest. Scale bar is 400µm. RIGHT: Representative brightfield images of wild-type and TET2-mutant AMs exposed to PBS or 12.5µg/mL $PM_{2.5}$ before harvest. Scale bar is 400µm.

E. Quantification of IM yield (IMs/mL) in wild-type and TET2-mutant co-cultures exposed to PM. t-test.

F. Quantification of AM yield (AMs/mL) in wild-type and TET2-mutant co-cultures exposed to PBS or PM. One-way ANOVA, post-hoc Tukey.

Error bars indicate mean ± SEM.

C. TET2-mutant bone marrow transplantation alters EGFR+ tumor architecture

In the in-vivo model of CHIP in NSCLC tumor-bearing animals, tumor burden was quantified as the density of EGFR+ cells per mm^2 (Figure 7A). TET2-mutant lung sections displayed a numerically higher EGFR+ density compared to wild-type controls, but this difference was not statistically significant (Welch's $t(3.64)=1.78$, $p=0.157$, $\eta^2=0.47$). Unlike the wild-type samples, the TET2-mutant condition exhibited intra-cohort variability, with high (red) and low tumor burden (green) phenotypes observed and annotated accordingly.

Based on heterogeneity in tumor lesion morphology, EGFR+ architecture (Compact A, Compact B, Disperse, Non-EGFR+) was also compared between wild-type and TET2-mutant samples. In Figure 7B, the cross-sectional area of the lesions is markedly higher in Compact B than Compact A ($t(29.92)=3.21$, $p=0.0031$, $\eta^2=0.257$). Additionally, differences were observed in the EGFR+ architecture and composition across BM transplant genotypes. Despite lacking statistical significance at n=4 sample size, TET2-mutant samples trended toward a lower proportion of Compact A cells (1.31% vs. 30.7% in wild-type) and a higher proportion of disperse cells (74.2% vs. 50.5% in wild-type) (Figure 7C). Figure 7D provides representative images of the annotated lung sections, illustrating lesion size and composition across wild-type and TET2-mutant (low and high tumor burden) samples.

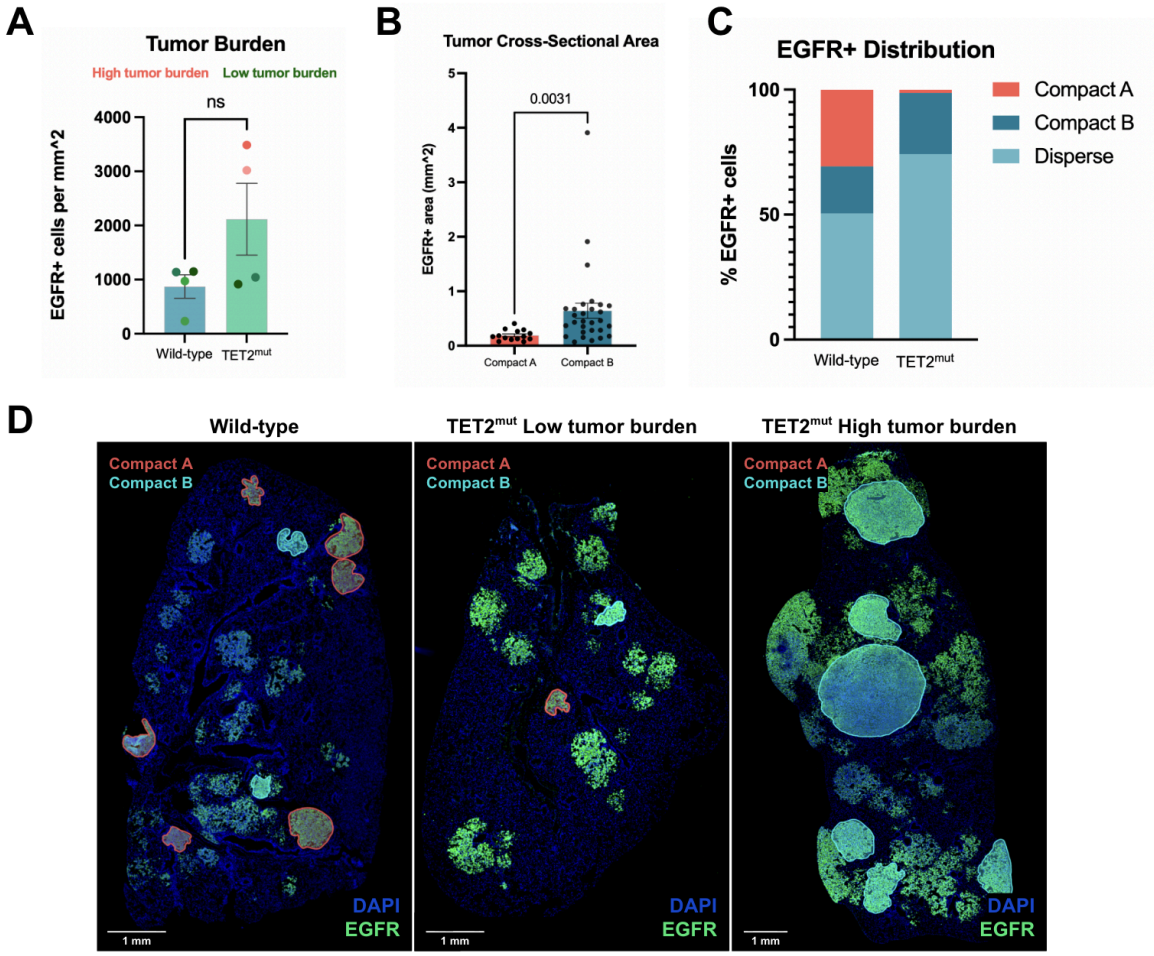

Figure 7. Morphological characterization of EGFR+ tumor burden

A. Quantification of tumor burden measured as EGFR+ cells per mm^2 in single-lobe wild-type and TET2-mutant lung sections. Data points stratified into high tumor burden (red) and low tumor burden (green) status. ns = not significant. t-test.

B. Lesion EGFR+ cross-sectional area (mm^2) for all distinct Compact A and Compact B annotations. t-test.

C. Stacked bar graph illustrating the averaged proportion of EGFR+ cells in Compact A, Compact B, and Disperse regions across wild-type and TET2-mutant samples.

D. Representative immunofluorescent, whole-lobe lung sections of wild-type and low and high tumor burden TET2-mutant samples. Compact A lesions outlined in red; Compact B outlined in cyan. Scale bar is 1mm.

Error bars indicate mean ± SEM.

D. TET2 mutations modify myeloid compartment and spatially exclude alveolar macrophages

Multiplex fluorescent staining of lung sections facilitated classification of 5 distinct immune cell populations (AMs, IMs, T cells, monocytes, and neutrophils), excluding B cells and T cell subtypes. The distribution of the lung immune myeloid and T cell compartment by cell count is visualized in Figure 8A, with the myeloid distribution independently isolated in Figure 8B. While further analysis of these patterns occur later in Section D, TET2-mutant samples exhibited a reduction in the proportion of AMs across all regions, as well as expanded populations of monocytes and IMs. The TME was also notably T cell "cold" since T cells composed less than 25% of the lung immune population identified by the QuPath image analysis pipeline.

Investigating the localization of alveolar macrophages, Figure 8C compares the AM density (quantified as the number of CD68+ and CD11b- cells per mm^2) in Compact A lesion cores and margins to representative Disperse and Non-EGFR+ regions (One-way ANOVA $F(7,69)=20.53$, $p<0.0001$, $\eta^2=0.6756$). Both the interior and margin of the wild-type lesions had an elevated AM density with respect to the TET2-mutant interior ($p=0.0010$) and margin ($p=0.0142$). Fold change between the margin and interior of each lesion was also averaged; albeit nonsignificant, TET2-mutant lesions had a higher fold change mean of 1.653 compared to 0.9645 in wild-type, suggesting an AM-excluded pattern ($t(2.040)=0.8804$, $p=0.4700$, $\eta^2=0.2754$). Furthermore, in the wild-type mice, AM accumulation decreased in lesion-adjacent Disperse and Non-EGFR+ regions, representing an AM border surrounding the Compact A wild-type tumors. Similar trends persisted in the Compact B lesions (One-way ANOVA $F(7,99)=13.89$, $p<0.0001$, $\eta^2=0.4955$) (Figure 8D), with the AM density respectively greater in the interior ($p<0.0001$) and margin ($p=0.0002$) of the wild-type lesions as compared to the TET2-mutant samples. Alluding to AM exclusion in TET2-mutant lesions, the margin to interior fold change was also significantly higher in the TET2-mutant condition (2.038) than the wild-type condition (1.207) ($t(26.13)=3.535$, $p=0.0015$, $\eta^2=0.3236$). Additionally, an AM border was indicated in both wild-type and TET2-mutant Compact B lesions due to the significantly higher accumulation of AMs in the lesion margin with respect to the surrounding Non-EGFR+ regions. Figure 8E illustrates the described differences in AM density across the annotated regions.

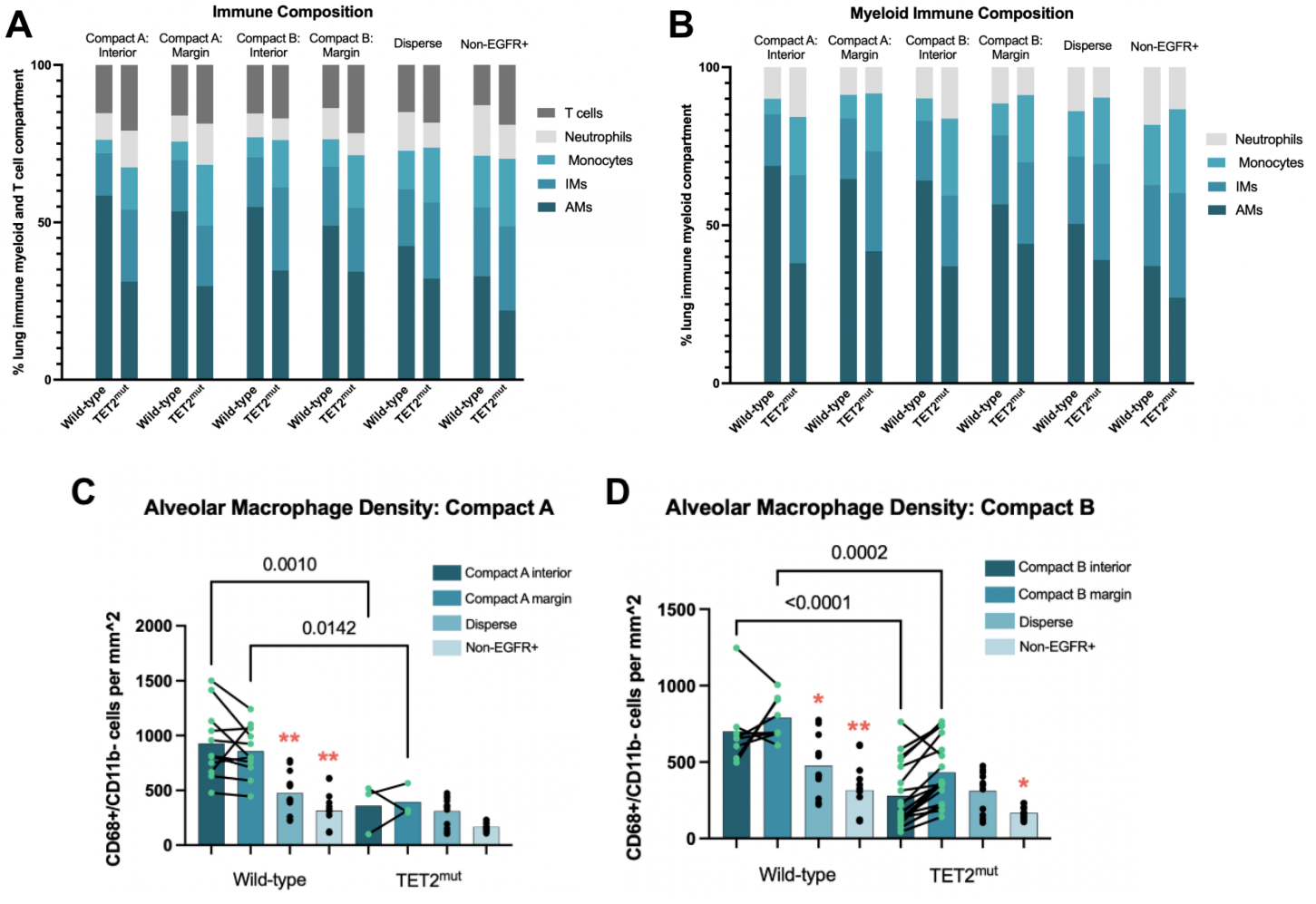

E

DAPI EGFR
CD68
CD11b
Overlay
COMPACT A
COMPACT B
DISPERSE
NON-EGFR+
Wild-type
TET2mut
100 µm

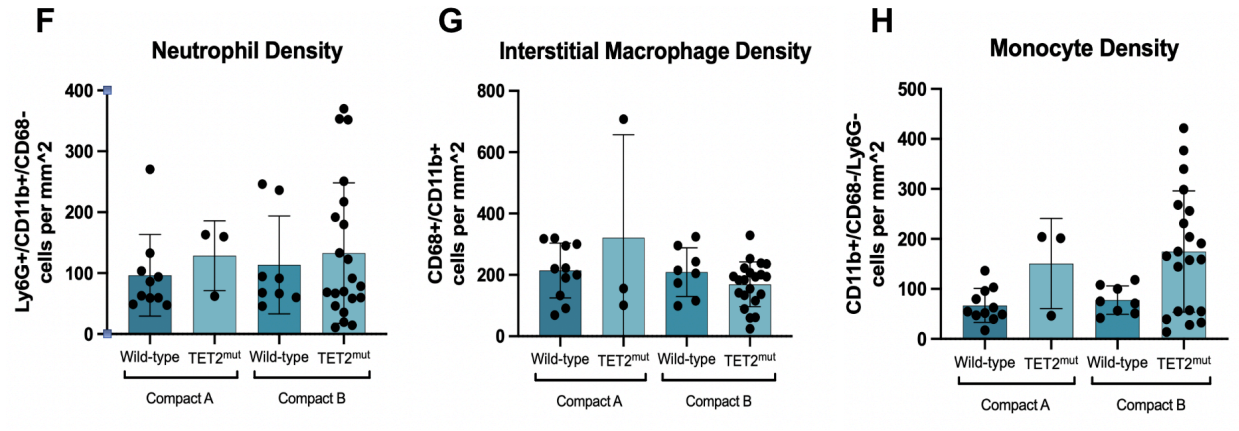

Figure 8. Immune TME compartmentalization and spatial heterogeneity in tumor-bearing lung sections

A. Stacked bar graph representing the proportions of immune subtypes, by raw cell count, in the lung immune myeloid and T cell compartments. Isolated into wild-type and TET2-mutant samples across the annotated regions: Compact A and B interior and margin, Disperse, and Non-EGFR+.

B. Stacked bar graph representing the proportions of immune subtypes, by raw cell count, in the lung immune myeloid compartment only. Isolated into wild-type and TET2-mutant samples across the annotated regions: Compact A and B interior and margin, Disperse, and Non-EGFR+.

C. Quantification of AM density (number of CD68+ and CD11b- cells per mm^2) in the interior and margin of wild-type and TET2-mutant Compact A lesions, as well as representative Disperse and Non-EGFR+ regions. Data points represent individual lesion annotations; connecting lines match lesion interior to its margin. ** indicates statistical significance ($p<0.05$) to both wild-type Compact A interior and margin. One-way ANOVA, post-hoc Tukey.

D. Quantification of AM density in the interior and margin of wild-type and TET2-mutant Compact B lesions, as well as representative Disperse and Non-EGFR+ regions. Data points represent individual lesion annotations; connecting lines match lesion interior to its margin. ** indicates statistical significance ($p<0.05$) to both wild-type Compact B interior and margin. * indicates statistical significance ($p<0.05$) to the wild-type or TET2-mutant Compact B margin, respectively. One-way ANOVA, post-hoc Tukey.

E. Representative fluorescent images of wild-type and TET2-mutant Compact A, Compact B, Disperse, and Non-EGFR+ regions, with overlay indicating AMs present in the lung section. White borders represent the internal and external bounds of the annotated margins. Scale bar is 100μm.

F. Measure of neutrophil density (number of Ly6G+, CD11b+, and CD68- cells per mm^2) across wild-type and TET2-mutant samples in Compact A and B lesion interiors. One-way ANOVA, post-hoc Tukey.

G. Measure of IM density (number of CD68+ and CD11b+ cells per mm^2) across wild-type and TET2-mutant samples in Compact A and B lesion interiors. One-way ANOVA, post-hoc Tukey.

H. Measure of monocyte density (number of CD11b+, Ly6G-, and CD68- cells per mm^2) across wild-type and TET2-mutant samples in Compact A and B lesion interiors. One-way ANOVA, post-hoc Tukey.

Error bars indicate mean ± SEM.

Figures 8F-8H compare the area densities of wild-type and TET-2-mutant neutrophils (One-way ANOVA $F(3,39)=0.061$, $p=0.9798$, $\eta^2=0.0047$), interstitial macrophages (One-way ANOVA $F(3,39)=1.907$, $p=0.1445$, $\eta^2=0.1279$), and monocytes (One-way ANOVA $F(3,39)=4.310$, $p=0.0032$, $\eta^2=0.2490$) in Compact A and B lesion interiors to investigate the compartmentalization of BM-derived immune cells. The densities were not significantly

different between wild-type and TET2-mutant samples, but apart from the IMs in Compact B lesions, neutrophils, IMs, and monocytes had numerically elevated densities in the TET2-mutant lesions.

IV. DISCUSSION

Lung cancer, particularly in never-smokers, is no longer regarded as a simple accumulation of mutations. Ranging from immune TME changes to environmental exposures to aging, the drivers of NSCLC are multifaceted and justify further investigation[12,19]. CHIP has recently emerged as a risk factor for NSCLC[6,7], and here, TET2-mutant CHIP is shown to enhance the proliferative capacity of lung macrophages and modify the immune TME composition and spatial organization, with trends toward impacting tumor growth.

Mutated TET2 has been shown to upregulate macrophage IL-1β expression and secretion[2,11], and exposure to an inflammatory stimulus, such as $PM_{2.5}$, may enhance this effect. Therefore, we asked whether increasing IL-1β concentration also increased tumor growth, using primary AT2 organoid OFE as a proxy. Informed by preliminary Swanton Lab cytokine assays, AT2 organoid cultures were treated on an IL-1β concentration gradient. Although the positive correlation between IL-1β concentration and OFE was nonsignificant, the linear regression along the gradient achieved statistical significance in cultures supplemented with 10ng/mL IFN-γ. IFN-γ is a cytokine predominantly produced by activated T and natural killer (NK) cells with context-dependent protumoral or antitumoral effects on alveolar epithelial cells[22]. Current work in the Swanton Lab provides evidence for T cell responses in PM-exposed animals with EGFR-mutant AT2 cells, as well as IFN-γ activation of macrophage populations, but T cell upregulation of IFN-γ may also have a negative, cytotoxic effect on mutant-AT2 growth. In the primary AT2 organoid cultures, 10ng/mL IFN-γ treatment proportionally suppressed organoid OFE; however, increasing IL-1β concentration partially compensated for the IFN-γ-associated decrease in OFE, suggesting biological distinctions in how the cytokines regulate AT2 proliferation.

Aligning with TET2 loss driving clonal expansion and myeloproliferation in-vivo, mouse recipients of TET2-mutant BM cells had elevated donor chimerism in the AM and IM immune compartments[3,10,20]. In addition to validating clonal hematopoiesis in vivo, indirect co-cultures of the plated IMs and AMs with primary AT2 organoids also modeled NSCLC tumor initiation and isolated the effects of immune secretions and paracrine signaling rather than cell-to-cell interactions between the plated immune cells and the AT2 cells and fibroblasts in the matrigel. Without the inclusion of immune cells, organoid outgrowth was limited in the PBS and PM controls; increases in OFE occurred upon the addition of either AMs or IMs. PM-exposed TET2-mutant IMs exhibited a significant increase in organoid formation respective to wild-type IMs. Due to harvest constraints, all IMs were treated with $PM_{2.5}$, so experimental replicates are necessary to investigate PM-driven initiation effects. In the indirect AM assays, there was not clear wild-type versus TET2-mutant distinction, but higher OFE *was* numerically attributed to PM exposure, implying differences in AM activation with the addition of exogenous inflammatory stimulus.

However, the experimental design of these co-cultures is a potential limitation; while all wells were plated with 50,000 IMs or AMs, genotype-dependent expansion of the plated immune cells throughout the experiment may have affected secretion concentrations. For instance, PM-exposed TET2-mutant IMs expanded significantly more than PM-exposed wild-type controls in vitro, which corresponds to the OFE results. Albeit statistically insignificant and less pronounced than the IM case, TET2-mutant AMs were also more proliferative; additionally, 12.5μg/mL $PM_{2.5}$ exposure suppressed yield in both genotypes. Wei et al. describes the cytotoxic effects of $PM_{2.5}$ treatment on AM viability, which may explain this modest decrease in expansion[21]. Interestingly, despite lower AM yield in the PM-treated wells, these samples still exhibited numerically higher OFE than PBS-treated AM controls. To contextualize the resultant differences in OFE, cytokine assays would be a suitable next step, as well as preparation of organoid assays that are indirectly and temporarily exposed to IMs and AMs to prevent expansion-associated

OFE modulation. Furthermore, a shortened experimental duration may reduce final organoid count, improving the accuracy of OFE quantification.

CHIP systemic impact on lung cancer was also approached from a progression perspective via the transplant of TET2-mutant BM cells into tumor-bearing mice. Here, the transplant of chimeric TET2-mutant HSPCs did not significantly augment tumor burden. A published KRAS model similarly observed no difference in burden[23]; however, the numerical trend toward increased TET2-mutant outgrowth and intra-cohort variability may instead reflect inconsistencies in the original tumor initiation method and artifacts of the small sample size (n=4). Upon definition and annotation of EGFR+ architectural subtypes, however, differences in lesion composition between wild-type and TET2-mutant samples were revealed. TET2-mutant samples were characterized by increased prevalence of Disperse EGFR+ regions and larger Compact B lesions, likened to a more advanced, aggressive, and proliferative state as compared to wild-type[24].

The wild-type and TET2-mutant immune compartmentalization within the lung tissue also differed. Of note, the immunostaining included neither B cells or T cell subtypes, which ought to be added in future experiments to more accurately represent the lung immune niche. Predominated by myeloid cells, the EGFR NSCLC model had a relatively T cell "cold" TME, without explicit localization to annotated regions of interest. Within the myeloid compartment, the TET2-mutant samples had lower proportions of AMs by cell count across all annotated regions, along with modest expansion of bone marrow-derived subtypes, such as IMs and monocytes. In part, this aligns with the findings of Pich et al., in which monocytes are recruited by lesions and aggregate as CD11b+ monocyte-derived IMs[12]. The current literature also describes the accumulation of tissue-resident alveolar macrophages near lesions during early tumor formation to stimulate epithelial-mesenchymal transition, followed by the redistribution of the AMs to the margin and an influx of monocyte-derived macrophages into the TME[25]. Not only does this correspond to the observed trends in immune composition, it reinforces the less advanced, less disperse EGFR+ architecture observed in the AM-rich, wild-type samples.

The AM immune niche exhibited the most spatial variability in density. In both Compact A and B lesions, the TET2-mutant interior and margin had lower AM density with respect to wild-type, consistent with the lower raw cell count proportions in Figures 8A and 8B. While the exact mechanism for the decreased AM accumulation remains unclear, it suggests suppressed migration of AMs to lesions or competitive migration of other immune subtypes. Despite a lack of significant difference in neutrophils, interstitial macrophages, and monocytes between TET2-mutant and wild-type lesion interiors, there was a trend toward greater density in the TET2-mutant conditions (excluding Compact B IMs). Frequently characterized in the literature[17], an alveolar macrophage border was also examined in this model, defined as a significant decrease in AM density from the lesion margin to the Non-EGFR+ "control," which was observed in all conditions except TET2-mutant Compact A (n=3 sample size attributed to lower Compact A proportion in TET2-mutant samples). The fold change between margin and associated interior was also compared; in the TET2-mutant Compact B lesions, the fold change was significantly greater than wild-type, implying an AM exclusionary phenotype. While the influence of a macrophage border is context-dependent, the aggregation of AMs in the periphery of a tumor is associated with inhibition of tumor immunity and promotion of tumor growth[26], further suggesting a more aggressive TET2-mutant phenotype.

In sum, the described organoid assays and murine model experiments highlight the systemic effects of somatic mutations in the HSPC compartment, with bone marrow-derived immune populations migrating to the lungs and modulating NSCLC initiation and progression. Future work remains necessary to mechanistically determine how TET2-mutant immune cells modify proinflammatory, protumorigenic signaling pathways and preferentially compartmentalize within lung tissue. Such insight into the CHIP-driven immune microenvironment serves to inform the treatment of NSCLC and other CHIP-associated disorders.

REFERENCES

[1] Jaiswal, S., & Ebert, B. L. (2019). Clonal hematopoiesis in human aging and disease. *Science (New York, N.Y.)*, *366*(6465), eaan4673. https://doi.org/10.1126/science.aan4673

[2] Buttigieg, M. M., & Rauh, M. J. (2023). Clonal hematopoiesis: Updates and implications at the solid tumor-immune interface. *JCO Precision Oncology*, *7*, e2300132. https://doi.org/10.1200/PO.23.00132

[3] Jaiswal, S., Fontanillas, P., Flannick, J., Manning, A., Grauman, P. V., Mar, B. G., Lindsley, R. C., Mermel, C. H., Burtt, N., Chavez, A., Higgins, J. M., Moltchanov, V., Kuo, F. C., Kluk, M. J., Henderson, B., Kinnunen, L., Koistinen, H. A., Ladenvall, C., Getz, G., … Ebert, B. L. (2014). Age-related clonal hematopoiesis associated with adverse outcomes. *The New England Journal of Medicine*, *371*(26), 2488–2498. https://doi.org/10.1056/NEJMoa1408617

[4] Buttigieg, M. M., Vlasschaert, C., Bick, A. G., Vanner, R. J., & Rauh, M. J. (2025). Inflammatory reprogramming of the solid tumor microenvironment by infiltrating clonal hematopoiesis is associated with adverse outcomes. *Cell Reports Medicine*, *6*(3), 101989. https://doi.org/10.1016/j.xcrm.2025.101989

[5] Wong, W. J., Emdin, C., Bick, A. G., Zekavat, S. M., Niroula, A., Pirruccello, J. P., Dichtel, L., Griffin, G., Uddin, M. M., Gibson, C. J., Kovalcik, V., Lin, A. E., McConkey, M. E., Vromman, A., Sellar, R. S., Kim, P. G., Agrawal, M., Weinstock, J., Long, M. T., … Natarajan, P. (2023). Clonal haematopoiesis and risk of chronic liver disease. *Nature*, *616*(7958), 747–754. https://doi.org/10.1038/s41586-023-05857-4

[6] Kessler, M. D., Damask, A., O'Keeffe, S., Banerjee, N., Li, D., Watanabe, K., Marketta, A., Van Meter, M., Semrau, S., Horowitz, J., Tang, J., Kosmicki, J. A., Rajagopal, V. M., Zou, Y., Houvras, Y., Ghosh, A., Gillies, C., Mbatchou, J., White, R. R., … Jorgenson, E. (2022). Common and rare variant associations with clonal haematopoiesis phenotypes. *Nature*, *612*(7939), 301–309. https://doi.org/10.1038/s41586-022-05448-9

[7] Tian, R., Wiley, B., Liu, J., Zong, X., Truong, B., Zhao, S., Uddin, M. M., Niroula, A., Miller, C. A., Mukherjee, S., Heiden, B. T., Luo, J., Puri, V., Kozower, B. D., Walter, M. J., Ding, L., Link, D. C., Amos, C. I., Ebert, B. L., … Cao, Y. (2023). Clonal hematopoiesis and risk of incident lung cancer. *Journal of Clinical Oncology*, *41*(7), 1423–1433. https://doi.org/10.1200/JCO.22.00857

[8] Sung, H., Filho, A. M., Laversanne, M., Ferlay, J., Siegel, R. L., Soerjomataram, I., Jemal, A., & Bray, F. (2026). Global cancer statistics 2024: GLOBOCAN estimates of incidence and mortality worldwide for 34 cancers in 186 countries. *Ca*, *76*(4), e70090. https://doi.org/10.3322/caac.70090

[9] Steensma, D. P., Bejar, R., Jaiswal, S., Lindsley, R. C., Sekeres, M. A., Hasserjian, R. P., & Ebert, B. L. (2015). Clonal hematopoiesis of indeterminate potential and its distinction from myelodysplastic syndromes. *Blood*, *126*(1), 9–16. https://doi.org/10.1182/blood-2015-03-631747

[10] Jiang, S. (2020). Tet2 at the interface between cancer and immunity. *Communications Biology*, *3*, 667. https://doi.org/10.1038/s42003-020-01391-5

[11] Belizaire, R., Wong, W. J., Robinette, M. L., & Ebert, B. L. (2023). Clonal haematopoiesis and dysregulation of the immune system. *Nature Reviews. Immunology*, *23*(9), 595–610. https://doi.org/10.1038/s41577-023-00843-3

[12] Pich, O., Bernard, E., Zagorulya, M., Rowan, A., Pospori, C., Slama, R., Encabo, H. H., O'Sullivan, J., Papazoglou, D., Anastasiou, P., Iliakis, C. S., Clark, S.-A., Dijkstra, K. K., Barbè, V., Bailey, C., Stonestrom, A. J., Enfield, K. S. S., Green, M., Brierley, C. K., … Swanton, C. (2025). Tumor-infiltrating clonal hematopoiesis. *The New England Journal of Medicine*, *392*(16), 1594–1608. https://doi.org/10.1056/NEJMoa2413361

[13] Nguyen, Y. T. M., Fujisawa, M., Nguyen, T. B., Suehara, Y., Sakamoto, T., Matsuoka, R., Abe, Y., Fukumoto, K., Hattori, K., Noguchi, M., Matsubara, D., Chiba, S., & Sakata‐Yanagimoto, M. (2021). Tet2 deficiency in immune cells exacerbates tumor progression by increasing angiogenesis in a lung cancer model. *Cancer Science*, *112*(12), 4931–4943. https://doi.org/10.1111/cas.15165

[14] Enfield, K. S. S., Colliver, E., Lee, C., Magness, A., Moore, D. A., Sivakumar, M., Grigoriadis, K., Pich, O., Karasaki, T., Hobson, P. S., Levi, D., Veeriah, S., Puttick, C., Nye, E. L., Green, M., Dijkstra, K. K., Shimato, M., Akarca, A. U., Marafioti, T., … Angelova, M. (2024). Spatial architecture of myeloid and T cells orchestrates immune evasion and clinical outcome in lung cancer. *Cancer Discovery*, *14*(6), 1018–1047. https://doi.org/10.1158/2159-8290.CD-23-1380

[15] Kaner, J., Desai, P., Mencia-Trinchant, N., Guzman, M. L., Roboz, G. J., & Hassane, D. C. (2020). Clonal hematopoiesis and premalignant diseases. *Cold Spring Harbor Perspectives in Medicine*, *10*(4), a035675. https://doi.org/10.1101/cshperspect.a035675

[16] Qin, W., Brands, X., Matsumoto, H., Butler, J. M., van't Veer, C., de Vos, A. F., Roelofs, J. J. T. H., Scicluna, B. P., & van der Poll, T. (2021). Role of myeloid tet methylcytosine dioxygenase 2 in pulmonary and peritoneal inflammation induced by lipopolysaccharide and peritonitis induced by escherichia coli. *Cells*, *11*(1), 82. https://doi.org/10.3390/cells11010082

[17] Buttigieg, M. M., Vlasschaert, C., Pershad, Y., Lanktree, M., Aldrich, M. C., Rauh, M. J., & Bick, A. G. (2026). Air pollution modifies clonal hematopoiesis-associated non–small cell lung cancer risk in nonsmoking individuals. *JNCI: Journal of the National Cancer Institute*, djag159. https://doi.org/10.1093/jnci/djag159

[18] Hill, W., Lim, E. L., Weeden, C. E., Lee, C., Augustine, M., Chen, K., Kuan, F.-C., Marongiu, F., Evans, E. J., Moore, D. A., Rodrigues, F. S., Pich, O., Bakker, B., Cha, H., Myers, R., van Maldegem, F., Boumelha, J., Veeriah, S., Rowan, A., … Swanton, C. (2023). Lung adenocarcinoma promotion by air pollutants. *Nature*, *616*(7955), 159–167. https://doi.org/10.1038/s41586-023-05874-3

[19] Swanton, C., Bernard, E., Abbosh, C., André, F., Auwerx, J., Balmain, A., Bar-Sagi, D., Bernards, R., Bullman, S., DeGregori, J., Elliott, C., Erez, A., Evan, G., Febbraio, M. A., Hidalgo, A., Jamal-Hanjani, M., Joyce, J. A., Kaiser, M., Lamia, K., … Hanahan, D. (2024). Embracing cancer complexity: Hallmarks of systemic disease. Cell, 187(7), 1589–1616. https://doi.org/10.1016/j.cell.2024.02.009

[20] Moran-Crusio, K., Reavie, L., Shih, A., Abdel-Wahab, O., Ndiaye-Lobry, D., Lobry, C., Figueroa, M. E., Vasanthakumar, A., Patel, J., Zhao, X., Perna, F., Pandey, S., Madzo, J., Song, C., Dai, Q., He, C., Ibrahim, S., Beran, M., Zavadil, J., … Levine, R. L. (2011). Tet2 loss leads to increased hematopoietic stem cell self-renewal and myeloid transformation. Cancer Cell, 20(1), 11–24. https://doi.org/10.1016/j.ccr.2011.06.001

[21] Wei, H., Yuan, W., Yu, H., & Geng, H. (2021). Cytotoxicity induced by fine particulate matter (PM2.5) via mitochondria-mediated apoptosis pathway in rat alveolar macrophages. Environmental Science and Pollution Research, 28(20), 25819–25829. https://doi.org/10.1007/s11356-021-12431-w

[22] Burke, J. D., & Young, H. A. (2019). IFN-γ: A cytokine at the right time, is in the right place. Seminars in Immunology, 43, 101280. https://doi.org/10.1016/j.smim.2019.05.002

[23] Parisi, T., Santibanez Ocampo, B., Adelman, J., Cai, Y., McConkey, M., Gibson, C. J., Ebert, B. L., Miller, P., & Jacks, T. (n.d.). Clonal hematopoiesis in lung adenocarcinoma pathogenesis. JCI Insight, 11(9), e203981. https://doi.org/10.1172/jci.insight.203981

[24] Moreira, A. L., Ocampo, P. S. S., Xia, Y., Zhong, H., Russell, P. A., Minami, Y., Cooper, W. A., Yoshida, A., Bubendorf, L., Papotti, M., Pelosi, G., Lopez-Rios, F., Kunitoki, K., Ferrari-Light, D., Sholl, L. M., Beasley, M. B., Borczuk, A., Botling, J., Brambilla, E., … Mino-Kenudson, M. (2020). A grading system for invasive pulmonary adenocarcinoma: A proposal from the International Association for the Study of Lung Cancer Pathology Committee. Journal of Thoracic Oncology, 15(10), 1599–1610. https://doi.org/10.1016/j.jtho.2020.06.001

[25] Casanova-Acebes, M., Dalla, E., Leader, A. M., LeBerichel, J., Nikolic, J., Morales, B. M., Brown, M., Chang, C., Troncoso, L., Chen, S. T., Sastre-Perona, A., Park, M. D., Tabachnikova, A., Dhainaut, M., Hamon, P., Maier, B., Sawai, C. M., Agulló-Pascual, E., Schober, M., … Merad, M. (2021). Tissue-resident macrophages provide a pro-tumorigenic niche to early NSCLC cells. Nature, 595(7868), 578–584. https://doi.org/10.1038/s41586-021-03651-8

[26] Ji, S., Shi, Y., & Yin, B. (2024). Macrophage barrier in the tumor microenvironment and potential clinical applications. Cell Communication and Signaling : CCS, 22, 74. https://doi.org/10.1186/s12964-023-01424-6

ACKNOWLEDGEMENTS

I wish to acknowledge Dr. Constandina Pospori and Dr. Charles Swanton for their guidance throughout my research project. I would also like to thank the MIT MISTI-UK program and the Laidlaw Scholars Program for their generosity in facilitating and funding this experience.